Research Article | Vol. 34, No. 20 / 5 Oct 2026 / Optics Express 38097
Optics EXPRESS

Deconvolution method for extreme ultraviolet broadband imaging spectrometry using dispersion-matched zone plates

MATS BRINKMAN,[1,2] OSCAR VERSOLATO,[1] IEVGENIIA BABENKO,[1] MARCELO ACKERMANN,[1,2] AND MUHARREM BAYRAKTAR[2,*]

[1]*Advanced Research Center for Nanolithography (ARCNL), Science Park 106, 1098 XG Amsterdam, The Netherlands*
[2]*Industrial Focus Group XUV Optics, MESA+ Institute for Nanotechnology, University of Twente, Drienerlolaan 5, 7522 NB Enschede, The Netherlands*
[*]*m.bayraktar@utwente.nl*

Abstract: We present a method to retrieve spectrally resolved spatial emission profiles using a broadband EUV imaging spectrometer with a tapered zone plate that is dispersion-matched to a transmission grating. Optical propagation simulations provide wavelength-dependent point spread functions used for forward modeling and deconvolution of tin-based laser-produced plasma emission images. Comparison with plasma sources of known size demonstrates recovery of effective source widths consistent with the diffraction-limited resolution of the instrument (15 µm) and shows clear improvement over, and a significant difference (up to a factor of 2 in emission area) to earlier fitting-based analysis. This work paves the way for adopting the concept of the broadband imaging spectrometer to diagnose plasma in academic and industrial settings.

© 2026 Optica Publishing Group under the terms of the Optica Open Access Publishing Agreement

1. Introduction

The performance of state-of-the-art extreme ultraviolet (EUV) lithography machines depends on the properties of the EUV light source, which is a laser-produced plasma (LPP) generated from tin microdroplets [1–4]. Such tin plasmas emit over a broad spectral range while peaking in the 13.5 nm ± 2% in-band region where multilayer mirrors (MLMs) efficiently reflect light [5]. Maximizing this in-band emission relative to out-of-band (the complement of the in-band region) components is essential, as radiation outside the narrow MLM bandwidth leads to collector mirror heating, ionization of ambient hydrogen gas, power loss, and, for longer wavelength ultraviolet emission, unwanted wafer exposure that can reduce imaging contrast [6,7]. A complete understanding of plasma emission therefore requires not only spectral information, but also information about the spatial distribution of the emission of a particular spectral component. Whereas previous studies have measured broadband LPP spectra, such spectra represent spatial averages and do not provide the emission distributions needed to understand etendue, optical transport, or the impact of changing plasma conditions on lithography performance [8,9].

Recently, Mostafa et al. [10] presented a novel imaging spectrometer operating across a broad 5–80 nm range. This device employs a transmission grating in series with a set of one-dimensional zone plates [11–16] that are individually matched (tapered) to a particular wavelength set by the grating dispersion [17], offering an easy-to-align tool with a large spectral range while maintaining sufficient spatial resolution of ~15 µm (defined here as the resolution in the object plane for point-to-point imaging, as compared to previous work [10,18] defining a 10 µm resolution in the focal plane) and spectral resolution of ~0.8 nm [17]. The combination of a broad spectral range and straightforward alignment makes the instrument a valuable tool for plasma diagnostics. In contrast to conventional zone-plate spectrometers optimized for a

#606992 https://doi.org/10.1364/OE.606992
Journal © 2026 Received 2 Jun 2026; revised 4 Sep 2026; accepted 11 Sep 2026; published 30 Sep 2026

Optics EXPRESS

single wavelength, the dispersion-matched design can be tailored to different wavelength ranges while maintaining imaging capability over a broad spectral bandwidth. Following up on this work, Babenko et al. [18] performed an experimental investigation on the spectral and spatial resolution of such an imaging spectrometer, concluding that both resolutions were in line with expectations. However, the analysis toward interpreting plasma emission size was done using an empirical multi-Gaussian fitting only part of the recorded image. This approach results in only an approximate size of the plasma, and not in a full spatial profile as required to fully and reliably describe the EUV source.

In this work, we present a method for retrieving the spectrally resolved spatial extent of an object from images recorded with an imaging spectrometer. To interpret the recorded images, we perform Rayleigh–Sommerfeld angular spectrum (RSAS) [19,20] simulations to compute wavelength-dependent point spread functions (PSFs). These are used for forward modeling and, in combination with a Richardson–Lucy algorithm, for deconvolution of the recorded images to obtain a full reconstruction of the spectrally resolved object. Our current experimental results benchmark the deconvolution approach, paving the way to adopt the concept of our imaging spectrometer to diagnose plasma in academic and industrial settings.

2. Experimental setup

In the following, we closely adhere to the description of Refs. [10,18]. Figure 1(a) shows a 3D schematic view of the setup, demonstrating the laser impacting a solid tin target, along with the operation of the imaging spectrometer. A 1-mm-thick poly-crystalline tin target is mounted onto a 2D translation stage in a vacuum chamber at 10^{-6} mbar. Using an Nd:YAG 1-µm laser, we irradiate the tin target at 10 Hz while regularly moving the stage to irradiate a new spot. The laser beam has a temporal FWHM of 6 ns and a spatial FWHM of 60 µm. We set the laser power density to 1.6×10^{11} W/cm^2 for the measurements shown in this work (cf. Reference [21]). In Fig. 1(b), the imaging axis is shown. At a distance of ≈ 3 mm an insertable slit with various sizes (10, 25 or 50 µm) is back-illuminated by the plasma, to control the effective plasma size. The mechanical slit width does not exactly correspond to the effective emitting profile. However, given the size of the plasma ($L \approx 100$ µm), the location of the backlighting plasma ($d_s = 3$ mm), and the slit thickness ($t_s = 12$ µm), the impact of penumbral broadening ($t_s L/d_s \approx 0.4$ µm), non-uniform illumination, and slit-width variations (± 0.5 µm) is limited. We estimate an overall uncertainty of ±1 µm in the effective source width taking these effects into account. At a distance $p_1 = 53$ cm, a 150 µm slit is used in combination with a 780-lines/mm transmission diffraction grating to disperse the light. The diffracted light impacts a set of 1D wavelength-tapered zone plates at a distance $p_2 = 5$ cm from the diffraction grating. The zone plates image the source onto a back-illuminated Greateyes (GE2048 512BI UV1) CCD at a distance $q = 110$ cm. This combination of distances results in a magnification $M = 1.9$ and a spectral resolution of 0.8 nm (at 13.5 nm). We show the design of the zone plate in Fig. 1(c). Along the diffraction axis, a series of 1D binary-amplitude zone plates is constructed, with each individual zone plate matching a specific wavelength as dispersed by the grating. The radius $r_{i,n}$ of the nth zone of the ith zone plate, dispersion-matched to the λ_i^{th} wavelength, is determined by

$$r_{i,n} = \sqrt{n\lambda_i \left(f + \frac{n\lambda_i}{4}\right)} \quad \text{with} \quad \lambda_i = d\frac{x_i}{\sqrt{p_2^2 + x_i^2}} \tag{1}$$

where f is the focal distance, d is the grating period of 1.3 µm (corresponding to the 780-lines/mm grating). The spatial resolution of the imaged source is determined by $\Delta w = \lambda f / 2r_N$. In the following, the number of zones N at each wavelength λ_i is set to achieve a constant spatial resolution across all wavelengths, $\Delta w = 15$ µm in the object plane. This design corresponds to an outermost zone width of 10 µm. The pixel size of the CCD camera is 13.5 µm, which is less

Optics EXPRESS

than half the effective spatial resolution in the image plane (≈ 29 µm) and thus samples above the Nyquist rate. This oversampling renders effects of the camera's finite resolution negligible. The imaging spectrometer is mounted at 30° relative to the laser propagation direction as shown in Fig. 1(a). A single CCD frame covers an approximate 25-nm wavelength range. By moving the CCD around the diffraction grating, multiple images can be stitched to cover a broad spectral range (5–80 nm). In all data presented here, dark frames (images with the same integration time, without irradiating the target) are taken and subtracted from the images, to perform a background subtraction correcting for the dark current of the CCD.

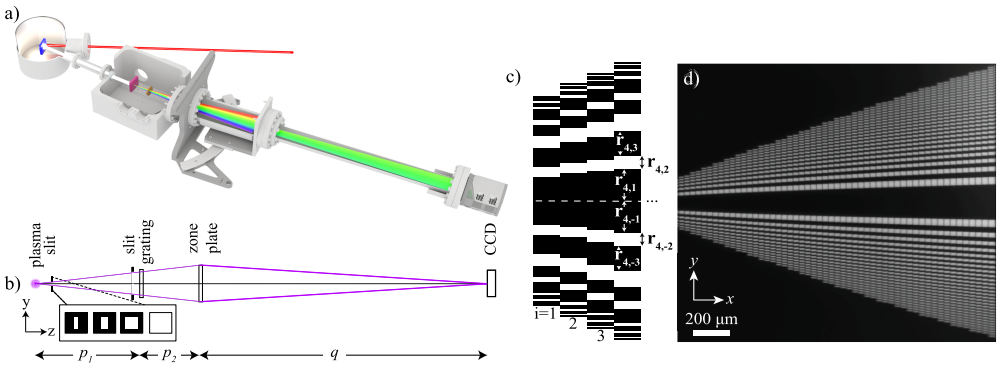

Fig. 1. (a) Schematic 3D overview of the experimental setup. (b) Side view showing the imaging axis (y). (c) A schematic of the dispersion-matched zone plate design where index i indicates the zone plate number in the dispersion axis. The radius $r_{i,n}$ of the nth zone of the ith zone plate is given in the text. (d) Optical microscopy image of the tapered zone plate designed for the range 5–80 nm. Figure adapted from Ref. [10] and modified for the present work.

3. Simulation of point spread function

Due to the complicated diffraction profile of a zone plate, numerical simulations of the light propagation through the setup are necessary for interpretation of the experimental data. We simulate this propagation using the RSAS method. Where we follow the adaptation of the angular spectrum method by Matsushima and Shimobaba [19], expanded on in Ref. [22] for diffraction by a zone plate. The Rayleigh-Sommerfeld equation [23] for a monochromatic source field $g(x, y, z)$ propagating along the z-direction is given as

$$g\left(x, y, z_0\right) = \iint g\left(x', y', 0\right) \frac{e^{i2\pi r' \lambda^{-1}}}{r'} \frac{z_0}{r'} \left(\frac{1}{2\pi r'} + \frac{1}{i\lambda}\right) dx' dy', \tag{2}$$

where $r' = \sqrt{(x - x')^2 + (y - y')^2 + z_0^2}$ and $z = 0$ and $z = z_0$ denote the source and observation planes, respectively. In contrast to the previous plane-wave approximation of Mostafa et al. [10], here we introduce a point source at a distance $p = p_1 + p_2$ away from the zone plate, necessary for a description of point-to-point imaging. A single propagation step from a point source of wavelength λ_0 at $z = 0$ to the zone plate at $z = 0.58$ m is done using Eq. (2) and then a binary mask representing the zone plate corresponding to λ_0 is applied using standard equations for zone plates cf. Eq. (1). A second propagation step is performed from the zone plate to the image plane. By executing the plane-to-plane propagation simulations for a number of distances between $z = 0$ to $z = 2.5$ m away from the source, a complete quasi-3D picture of the propagation can be constructed. In Fig. 2(a), a side-view of this simulation is shown, where a point source of light at $\lambda = 13.5$ nm propagates to a zone plate designed for such a wavelength with 17 zones,

Optics EXPRESS

a focal length of $f = 0.380$ m and spatial resolution of 15 µm. The influence of the grating on the source field along the imaging axis is expected to be small, since only the support bars of the grating diffract light and their diffraction amplitude is small [17]. This effect is therefore neglected in the present simulations. The resulting diffraction profile is a superposition of the first diffraction order, which forms the main focal spot at the CCD plane, and the other odd diffraction orders (since even orders are suppressed for a binary zone plate with a 50% duty cycle) leading to lower intensity side-peaks away from the center. Higher order foci are also observed at integer fractions of the imaging focal distance. A 1D line out of the imaging plane ($z = 1.68$ m) is shown in Fig. 2(b), where a sharp triple peak of the 1st order diffraction and a set of broader peaks can be observed as a result of the zeroth order of the different zones. The central peak has a FWHM of approximately 29 µm in the image plane, consistent with a 15 µm object-plane resolution and a magnification of 1.9. At larger off-axis positions, the simulated PSF is non-zero because of residual contributions from higher odd diffraction orders. These off-axis contributions, of the zeroth and odd higher orders, could be filtered out using an order-sorting aperture; however, for the method developed in section 5, the full diffraction pattern gives more information on the original source, as compared to one with an order sorting aperture blocking part of this pattern. Using the simulated point spread function (PSF), one can develop a better understanding of the non-diffraction-limited blurring due to design parameters of the optical setup. The accuracy of the reproduction of the experimental PSF by the simulated PSF is critical when making comparisons between experiment and simulation. In the following, we approximate the simulated PSF as shift invariant over the expected source-size range of approximately 100 µm. This approximation is justified by the small angular field of view of the zone plate, 0.2 mrad, for which spatial variations in the PSF are negligible. When attempting to model significantly larger or more off-axis features, a spatially dependent PSF-model should be used. To simulate a finite size source, the intensity PSF (H) can be convolved with the intensity of an object (O) to determine the image intensity (I) of that object in the imaging plane [20]

$$I = H * O, \tag{3}$$

since the plasma light considered here is incoherent, given the thermal population in the plasma of the wide range of atomic levels in highly charged tin ions [24] leading to near-Planckian radiation [25]. To correct for the effect of polychromaticity of the light impinging on a zone plate due to the finite spectral resolution of the grating, simulations are done for a band of wavelengths and averaged (assuming a Gaussian distribution) to find the blurring of the PSF. Simulating

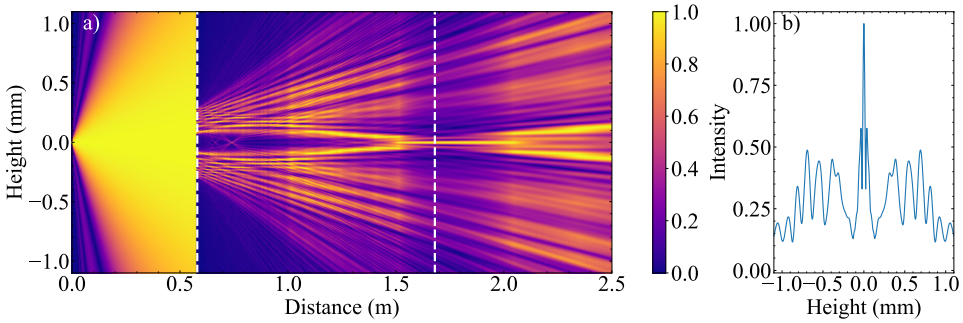

Fig. 2. Simulated intensity propagation profile of $\lambda = \$13.5$ nm light. (a) A side-view of the propagation through the optical setup as shown in Fig. 1(b), with a point source at $z = 0$ m, the zone plate at $z = 0.58$ m, with a total height of 0.6 mm, beyond which light is blocked out. The CCD plane is located at $z = 1.68$ m, normalized per propagation distance. (b) A lineout of the optical response of the system at the CCD plane.

Optics EXPRESS

optical propagation using RSAS and applying this equation to propagate light from any source through the optical setup should give good agreement to experiment, as long as the PSF and the object/source are well known.

4. Convolution

Figure 3(a) shows a wavelength-dependent image of the plasma recorded in the 5–80 nm range as diffracted by the dispersion-matched zone plate, normalized with respect to the spectrum. The image shows a prominent central band, from the first diffraction order of the zone plate, and multiple features on the side of the central band resulting from other diffraction orders, as shown in Fig. 2. Immediately off-axis, the zeroth diffraction order is the most prominent contribution. Further off-axis, up to $\lambda = 50$ nm, cutoff at higher wavelength due to the limited size of the CCD chip, the higher diffraction order contributions are observed. The diffraction profile shows a clear broadening with increasing wavelength; both in its central feature, due to the expected increase in emission size [10], and in its off-axis features, due to the combination of the aforementioned broadening and the tapering of the zone plate [see Fig. 1(d)]. The zone plate's nth diffraction order of an mth grating diffraction order will coincide with the first orders on the CCD for $n = m$ (since the focal distance $f_n \approx r_N^2/n\lambda$). The focusing efficiency of the higher orders is lower and the depth of focus (λ/NA^2) is shorter for the higher order than for the first order, leading to larger off-axis contributions due to chromatic aberrations (see Appendix for more details). The prominent contributions of the higher orders are those originating from the 13.5-nm peak observed at 40.5 and 67.5 nm in the experimental image. In the experimental image the lower focusing efficiency and the corresponding higher relative intensity of the off-center features as expected from simulations are clearly visible.

Simulations using RSAS as described in section 3 are performed for the same wavelengths and zone plate as experimentally measured to find PSFs for these parameters. These are then convolved with a Gaussian function with variable FWHM, which are fitted, using a non-linear least squares method, to the experimental image (the FWHM value being the sole free-fit parameter in the procedure). The results of this wavelength-dependent fitting are shown in Fig. 3(b). Using this one-parameter fit, similar features as described before are seen in the simulation image. The largest qualitative difference is the depth of the dip next to the central peak, which is much deeper in simulation as compared to the experiment, and the background in the experimental image, which is higher because of scattering contributions. To better study the agreement between experiment and simulation, lineouts at specific wavelengths corresponding to dashed lines in panels (a) and (b) are shown in the same color in panels (c-g). Considering only first-order contributions of the grating dispersion leads to good agreement for wavelengths where there are no higher orders of the main emission peak expected, namely below ~40 nm cf. panels (c-e). The central peak has a similar shape in both experiment and simulation. However, the dip between this central band and the off-center peaks is deeper for the shorter wavelengths, improving slightly for the longer wavelengths. The individual peaks in the off-axis contributions match reasonably well between experiment and simulation, with slight differences most likely due to experimental imperfections including scattering.

In panels (f) and (g), calculating only first orders (black lines) clearly does not sufficiently well reproduce the experiment. Taking into account higher orders, however, gives much better agreement. This better agreement derives mainly from the increased relative intensity of the off-center peaks, as expected from the treatment in the Appendix. Both the simulated central peak and adjacent dips agree well with experiment in terms of both intensity and location. However, even considering higher order contributions, agreement for the peaks in the off-axis zeroth order is worse than for shorter wavelengths. These discrepancies are likely due to experimental aspects that are not considered in simulations, e.g., any manufacturing tolerances of the zone plate, a systematic minor misalignment, or a deviation in the diffraction efficiency of the grating for

Optics EXPRESS

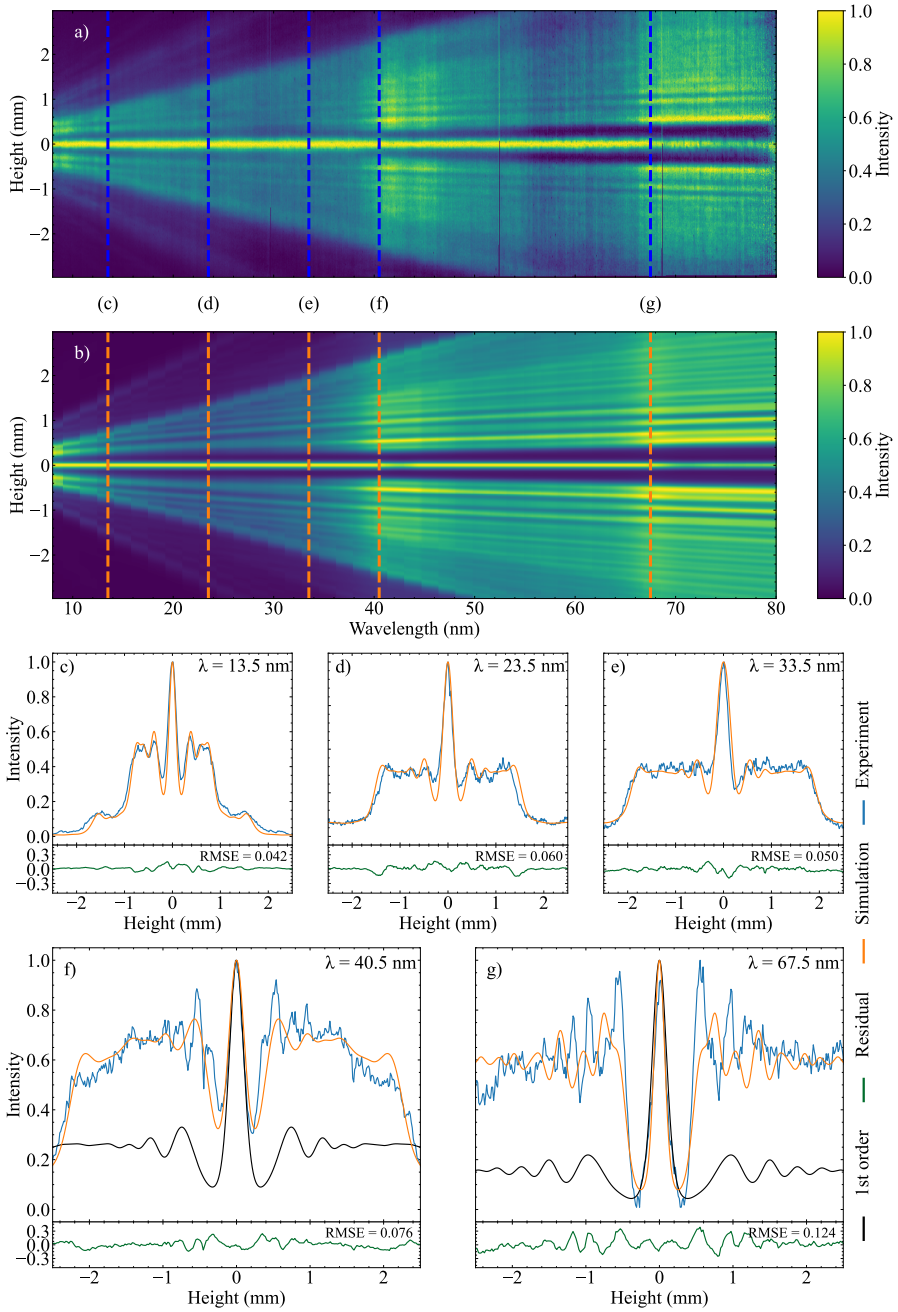

Fig. 3. Comparison of experimental results and simulation. (a) CCD image as recorded in the experiment, normalized by the spectrum, with overlaying lines at regions of interest. (b) Simulated image as described in the main text, normalized by the spectrum, with overlaying lines at regions of interest. Panels (c–g) show vertical lineouts of data shown in panels (a,b), where the color of the overlying line matches the color of the lineout. Panels (c–g) also include the respective residuals at the bottom (green curve); an overall root-mean-square-error (RMSE) value is also provided. In panels (f,g) an additional black line shows the simulation without taking into account the effect of higher orders from the dispersion grating.

Optics EXPRESS

higher diffraction orders (we here use the experimentally calibrated diffraction efficiencies of gratings [17,26]). Furthermore, fixing the plasma shape to be Gaussian does not allow for fitting of asymmetric or more sophisticated plasma emission profiles, which may lead to the observed discrepancies. Noise contributions are more significant at longer wavelengths as a result of the decrease in absolute signal level leading to low brightness of these spectral regions. In the lower parts of panels (c–g), the residuals between the experimental and simulated data are shown, together with the overall RMSE averaged over the full diffraction pattern. The error increases by a factor of 3 between 13.5 and 67.5 nm. The residuals show an overall high-frequency noise level consistent with the measured background fluctuations of approximately 40 cnts/s (the shot noise is approximately 50 cnts/s (2%) at maximum; further contributions to background fluctuations include laser-energy variations). However, the dominant contribution to the residuals arises, at low frequencies, from local discrepancies in the depths and heights of the diffraction peaks which points towards the finite accuracy with which the simulated PSF reproduces the actual, experimental PSF. A quantitative analysis of the PSF accuracy, which would include 3D-effects, production imperfections, alignment variation, etc., is beyond the scope of the current study. An asymmetry in the image, which is most visible in panel (g), originates from a misalignment in the zone plate, most likely the result of the zone plate being mounted under an unavoidable finite tilt angle. This effect could be modeled by introducing an additional angular alignment parameter in the PSF simulation. However, because the asymmetry is apparent only in panel (g), and because such a correction would introduce additional model dependence, we instead treat it as a possible source of systematic uncertainty. From this comparison between the experimental and simulated images, we conclude that the simulations accurately capture both the propagation behavior and the spatial extent of the emitting plasma. Knowing that the methodology described in section 3 works well allows one to interpret experimental data using these simulations directly. The Gaussian fits of the different wavelength bands are informative in approximating an emission size for a plasma, but they do not give any information on the asymmetry or finer details of the source that can be extracted using a deconvolution approach as in the next section.

5. Deconvolution

To reconstruct the full spatial emission profile from experimental images, without resorting to fitting a Gaussian, Eq. (3) should be inverted to find an object. Many algorithms for deconvolution exist in the literature, where a standard solution for images with Gaussian and Poissonian noise is Richardson-Lucy deconvolution [27–30]. Richardson-Lucy deconvolution is an iterative maximum likelihood method, and thus finds the object by looking for the most likely object giving rise to the image. The standard update rule for Richardson-Lucy deconvolution is given as

$$O^{(n+1)} = O^{(n)} \odot \left(\frac{I}{O^{(n)} * H} * \overline{H} \right), \tag{4}$$

where $\overline{H}$ is the conjugate of the PSF, $O^{(n)}$ is the nth iteration step of the object O, for this work the initial guess for the object $O^{(0)} = I$ and $\odot$ denotes elementwise multiplication. Due to the ill-posedness of deconvolution, at some point during the iteration, noise artifacts start to dominate due to noise amplification. Choosing when to stop the deconvolution is thus sensitive to the signal to noise ratio of an image, which widely varies for different plasma conditions and wavelengths and, thus, defining a stopping criterion cannot be done generically. Various proposals to define this stopping criterion have been published in the literature [31,32]; however, for the deconvolution of 1D-lineouts with complicated PSFs, no solutions are available. In our specific case, it was found that the cumulative change between two iteration steps as in Eq. (5) has a minimum at some iteration number, where the reconstruction resembles the ground truth

Optics EXPRESS

well. This approach for choosing a stopping criterion is taken in this work.

$$n_{\text{stop}} = \arg\min\left(\sum_{\text{pixel}}\left|O^{(n)} - O^{(n-1)}\right|\right). \tag{5}$$

In the following, the experiments are done using slits as shown in Fig. 1(b), inserted inline with the spectrometer close to the plasma, thus fixing the effective plasma size to have a ground truth to compare the reconstruction to. To model these measurements, the PSF simulations included an additional aperture located 3 mm from the point source, corresponding to the slit position in the experiment. This accounts for the finite plasma-slit distance in the effective source definition. In Fig. 4(a-c), a typical deconvolution process is illustrated. In panel (a) a lineout of the experimental data at $\lambda = 13.5$ nm, with a 50 µm slit is shown. In panel (b) the PSF for $\lambda = 13.5$ nm is presented, and in panel (c) the deconvolution of the experiment by the PSF is demonstrated. The deconvolution yields a peaked profile with a slight asymmetry that cannot be captured by the Gaussian fitting method. However, features close to the diffraction limit should be interpreted with care, since the method cannot reliably resolve structures smaller than the diffraction limit. In addition, experimental uncertainties, particularly angular misalignment as discussed in Section 3, may produce similar apparent asymmetries in the reconstructed profiles.

In panels (d), (e), and (f) similar experiments are performed for the slit sizes 50, 25, and 10 µm, respectively. The FWHM values of these reconstructions are shown to find an approximation of the object size, which is expected to be close to the slit size. For the smallest slit, at 10 µm, the slit is smaller than the spatial resolution of the system of 15 µm, and thus this value is taken as the expected reconstruction size. The optimal number of Richardson-Lucy iterations, determined using Eq. (5), ranges from approximately 200 to 1000, depending on both wavelength and object size (see Visualization 1 for an example). Smaller reconstructed features generally require more iterations, whereas larger object sizes converge after fewer iterations [29]. The wavelength dependence of the optimum number of iterations is more difficult to interpret, because changes in the PSF shape and wavelength-dependent signal-to-noise ratio are coupled [30]. All measurements are also compared to results from a previous analysis method by Babenko et al. [18], which uses an empirical fitting of a set of triple-Gaussians (including an offset) to the central band of the image. From panels (d-f) it is clear that the deconvolution method reproduces the expected source sizes significantly more accurately than the earlier triple-Gaussian fitting method, due to a much better inclusion of the underlying diffraction effects. The triple-Gaussian fit does not account for contributions from neighboring diffraction features, which can bias the recovered source size toward either larger or smaller values. Panel (f) shows that the deconvolution method can recover features consistent with the diffraction limit. Uncertainties in the recovered FWHM values are estimated from three contributions: the variation in retrieved size within a 1 nm wavelength band, the sensitivity to the Richardson-Lucy stopping criterion evaluated by varying the number of deconvolution iterations by ±10% around optimum, and the uncertainty associated with the wavelength used in the simulated PSF, evaluated over ±0.5 nm. These contributions are added in quadrature. The uncertainty band for the slit sizes is taken to be 1 µm, as described in Section 2. The uncertainties in the fitting results are taken directly from Ref. [18]. Given this success in reproducing the ground truth source sizes, in panels (g) and (h) the same method is used to find respectively the actual shape and FWHM of a plasma without a slit. In panel (g), there are some fluctuations in the absolute location of the center of the peak as the deconvolution method allows some freedom in the location of the maximum intensity which does not impact the size estimates. Indeed, the general trend of the $1/e^2$ contour shows that the plasma size increases as a function of wavelength, as expected. The same trend can be observed in the FWHM plot in panel (h), where a linear growth in plasma emission size as a function of wavelength is found similar to fitting method. From the comparison between the reconstruction and fitting approaches,

Optics EXPRESS

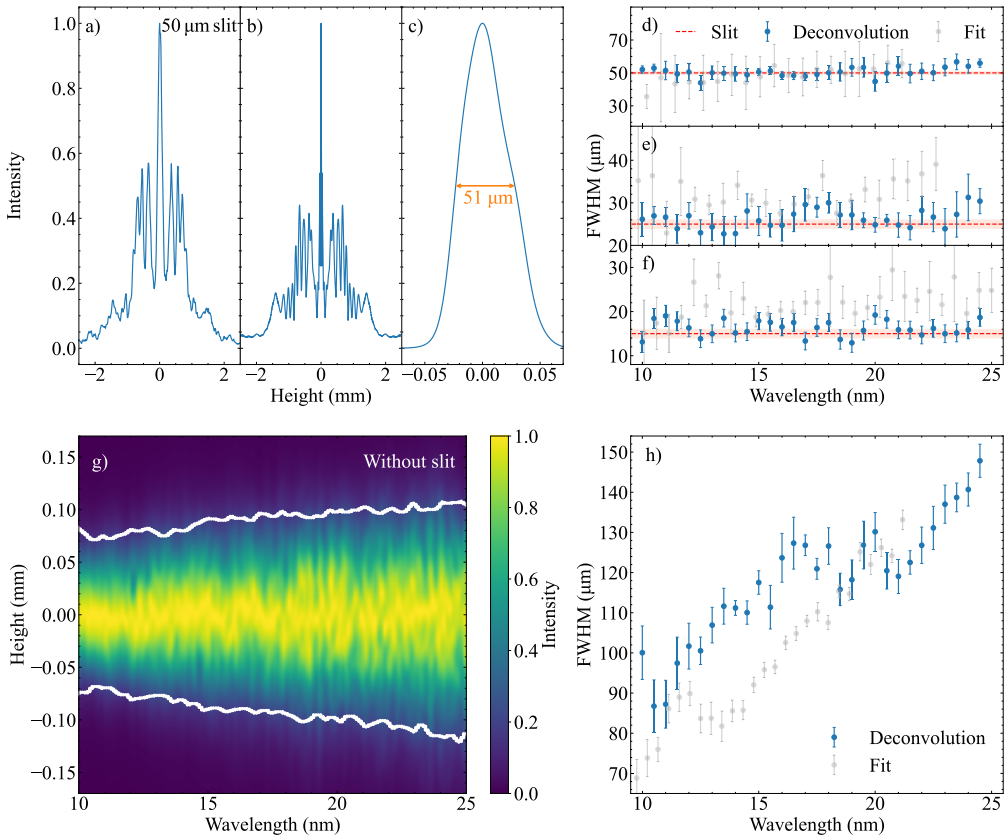

Fig. 4. Deconvolution method and results. (a) Experimental lineout at λ = 13.5 nm wavelength with a 50 µm slit inline with plasma. (b) PSF at the same wavelength as described in Section 3. (c) Deconvolution of the experimental lineout in panel (a) by the PSF in panel (b). (d–f) Comparison between FWHM of reconstruction in blue, established fitting technique of Ref. [18] in green, and the ground truth in red, for plasmas with additional 50, 25 and 10 µm slits (d, e, and f, respectively). (g–h) Wavelength-dependent deconvolution and FWHM of experimental image without an additional slit in front of the plasma. White contours indicate the $1/e^2$ level.

Optics EXPRESS

two simple conclusions can be made. First, the interpretation of small features ($\leq 25\,\mu$m) and thus interpretation of up to diffraction limited data is much better for the reconstruction method than for the fitting method. Second, our reconstruction method highlights large differences in the apparent plasma emission area, comparing previous with the current analysis and, thus, in the apparent brightness. At wavelengths around 13.5 nm, the differences are up to nearly a factor of 2 in emission area as compared to the prior fitting method, significantly impacting the inferred brightness. Beyond improving the accuracy in size measurement, the reconstruction method provides full spatial profiles, allowing for the interpretation of non-Gaussian or asymmetric plasma shapes, provided that alignment-induced effects are minimized. LPPs generated by micro-droplets instead of planar targets, using long pulses, are expected to exhibit very asymmetric EUV emission profiles [33]. Imperfections in the laser beam may also lead to asymmetries important to the application cf. Reference [34].

6. Conclusion

We have demonstrated a method to extract spectrally resolved spatial emission profiles from broadband EUV imaging spectrometer data. Wavelength-dependent PSFs are obtained through Rayleigh–Sommerfeld Angular Spectrum simulations, which accurately reproduce the complex diffraction behavior of zone plates. By applying Richardson–Lucy deconvolution, the method is validated using slits backilluminated by a tin-based LPP source and spectrally dependent object reconstructions are shown. The reconstruction method significantly improves on earlier fitting-based analyses, resulting in source sizes that agree closely with known ground truth slit widths, consistent with the diffraction limit, and providing full spatial profiles rather than a single fitted width. Overall, this combined experimental–computational methodology improves the accuracy and interpretability of imaging spectrometer data. It allows for detailed spatial characterization of EUV plasma sources across a broad spectral range, offering a tool for optimizing source performance and improving understanding of underlying plasma physics. Future implementations could employ more advanced diffractive optical elements instead of the tapered binary amplitude zone plates used here. Phase or blazed zone plates could increase the overall throughput and direct a larger fraction of the incident light into the desired first diffraction order.

Appendix

To accurately simulate the effect of the higher diffraction orders of the grating on the observed pattern in the imaging plane, simulations of first, third, and fifth diffraction orders of the grating were performed for the wavelength range of 5–80 nm. As explained in the main text, the most impactful higher orders are those of 13.5 nm light, and thus at $13.5 \times 3 = 40.5$ and $13.5 \times 5 = 67.5$ nm on the dispersion axis. Because of the relative high intensities of these wavelengths full propagation simulations are shown for the 67.5 nm zone plate in Fig. 5. The side-view propagation panels (a–c) show a similar diffraction pattern as in Fig. 2 for the first diffraction order of 67.5 nm, the third diffraction order of 22.5 nm, and the fifth diffraction order of 13.5 nm light, respectively. Highlighted is also the variance in imaging plane as a result of the blurring in the PSF due to chromatic aberrations resulting from the dispersion grating. The major difference with increasing diffraction order is the narrowing of the depth of focus (DOF), as explained in the main text. The higher orders show that the DOF is narrower, which results in an increase in blurring due to chromatic aberrations of the diffracted light. In panels (d–f) it is shown that this results in a relative increase in the off-axis contributions of the zone plate diffraction to the intensity profile in the imaging plane. From this we conclude that to accurately simulate and interpret the workings of the imaging spectrometer, a combination of the PSFs for the first, third, and fifth orders, weighted by the intensity and the dispersion efficiency of the grating of these orders, should be used. Since the dispersion grating efficiencies are determined

Optics EXPRESS

experimentally [17], uncertainties in their calibration lead to corresponding uncertainties in the relative amplitudes of higher-order PSF contributions.

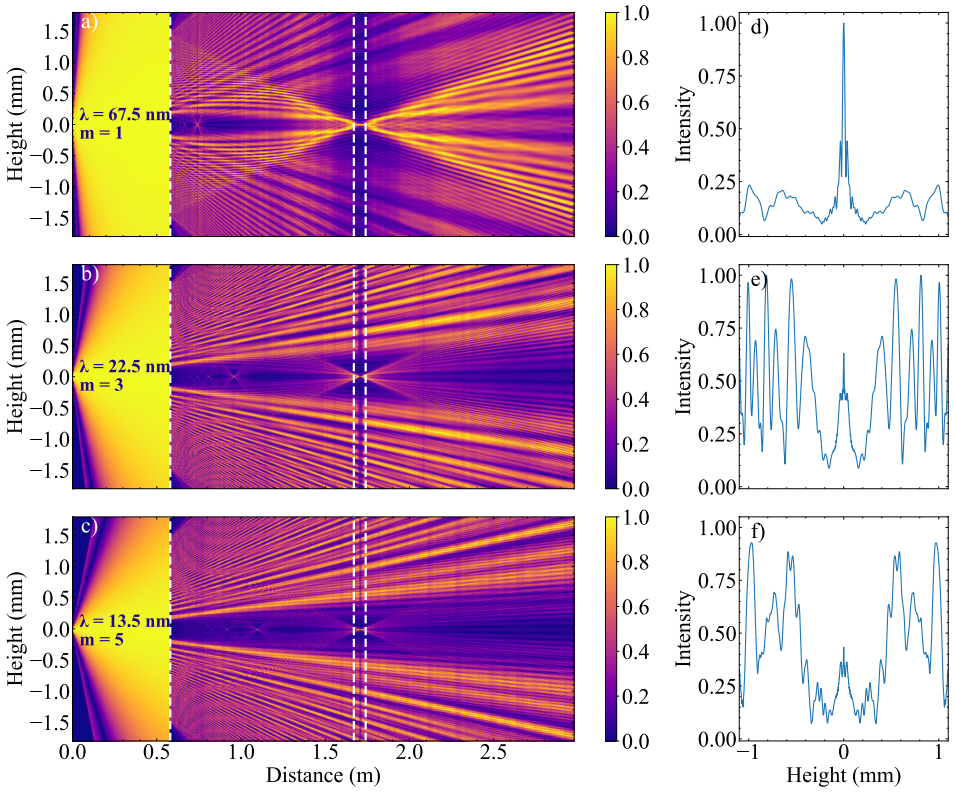

Fig. 5. Simulated intensity propagation profile of a zone plate designed for $\lambda = 67.5$ nm. (a–c) Side-views of the propagation through the optical setup similar to Fig. 2, with a point source of $\lambda = 67.5$, 22.5 and 13.5 nm, respectively, for panels (a), (b) and (c), at $d = 0$ m, the zone plate at $d = 0.58$ m and the imaging plane at $d = 1.67 - 1.74$ m, showing the variance in focal length over the spectral resolution. The zone plate in all panels is designed for 67.5 nm. (d–f) Lineouts of the optical response of the system at the imaging plane averaged for a band of wavelengths around the central wavelength corresponding to the spectral resolution of the grating.

Funding. Ministry of Economic Affairs and Climate Policy.

Acknowledgments. This work was conducted at the Advanced Research Center for Nanolithography (ARCNL), a public-private partnership between the University of Amsterdam (UvA), Vrije Universiteit Amsterdam (VU), Rijksuniversiteit Groningen (UG), the Dutch Research Council (NWO), and the semiconductor equipment manufacturer ASML and was partly financed by "Toeslag voor Topconsortia voor Kennis en Innovatie (TKI)" from the Dutch Ministry of Economic Affairs and Climate Policy. The transmission grating spectrometer and zone plates were developed in the Industrial Focus Group XUV Optics at the University of Twente. MB and OOV thank Stefan Witte for useful discussions.

Disclosures. The authors declare no conflicts of interest.

Data availability. Data underlying the results presented in this paper are not publicly available at this time but may be obtained from the authors upon reasonable request.

Optics EXPRESS

References

1. V. Y. Banine, K. N. Koshelev, and G. H. P. M. Swinkels, "Physical processes in EUV sources for microlithography," J. Phys. D: Appl. Phys. **44**(25), 253001 (2011).
2. M. Purvis, I. V. Fomenkov, A. A. Schafgans, *et al.*, "Industrialization of a robust EUV source for high-volume manufacturing and power scaling beyond 250 W," in *Extreme Ultraviolet (EUV) Lithography IX*, vol. 10583 K. A. Goldberg, ed., International Society for Optics and Photonics (SPIE, 2018), pp. 476–485.
3. H. Mizoguchi, H. Nakarai, T. Abe, *et al.*, "High power LPP-EUV source with long collector mirror lifetime for high volume semiconductor manufacturing," in *2018 China Semiconductor Technology International Conference (CSTIC)*, (2018), pp. 1–7.
4. O. O. Versolato, "Physics of laser-driven tin plasma sources of EUV radiation for nanolithography," Plasma Sources Sci. Technol. **28**(8), 083001 (2019).
5. Q. Huang, V. Medvedev, R. van de Kruijs, *et al.*, "Spectral tailoring of nanoscale EUV and soft x-ray multilayer optics," Appl. Phys. Rev. **4**(1), 011104 (2017).
6. K. Liu, Y. Li, F. Zhang, *et al.*, "Transient thermal and structural deformation and its impact on optical performance of projection optics for extreme ultraviolet lithography," Jpn. J. Appl. Phys. **46**(10R), 6568–6572 (2007).
7. G. Yang and Y. Li, "Analysis and control of thermal and structural deformation of projection optics for 22-nm EUV lithography," in *Extreme Ultraviolet (EUV) Lithography III*, vol. 8322 (International Society for Optics and Photonics, 2012), p. 83222V.
8. Z. Bouza, J. Byers, J. Scheers, *et al.*, "The spectrum of a 1-μm-wavelength-driven tin microdroplet laser-produced plasma source in the 5.5-265.5 nm wavelength range," AIP Adv. **11**(12), 125003 (2021).
9. M. A. van de Kerkhof, F. Liu, M. Meeuwissen, *et al.*, "High-power EUV lithography: spectral purity and imaging performance," J. Micro/Nanolithogr., MEMS, MOEMS **19**(03), 033801 (2020).
10. Y. Mostafa, Z. Bouza, J. Byers, *et al.*, "Extreme ultraviolet broadband imaging spectrometer using dispersion-matched zone plates," Opt. Lett. **48**(16), 4316–4319 (2023).
11. F. Döring, B. Rösner, M. Langer, *et al.*, "Multifocus off-axis zone plates for x-ray free-electron laser experiments," Optica **7**(8), 1007–1014 (2020).
12. J. O. Schunck, F. Döring, B. Rösner, *et al.*, "Soft x-ray imaging spectroscopy with micrometer resolution," Optica **8**(2), 156–160 (2021).
13. A. V. Baez, "Fresnel zone plate for optical image formation using extreme ultraviolet and soft x radiation," J. Opt. Soc. Am. **51**(4), 405–412 (1961).
14. F. Marschall, Z. Yin, J. Rehanek, *et al.*, "Transmission zone plates as analyzers for efficient parallel 2D RIXS-mapping," Sci. Rep. **7**(1), 8849 (2017).
15. L. E. Ocola, J. Maser, S. Vogt, *et al.*, "Tapered tilted linear zone plates for focusing hard x-rays," in *SPIE Proceedings*, vol. 5539 (SPIE, 2004), pp. 165–173.
16. K. Li and C. Jacobsen, "More are better, but the details matter: combinations of multiple Fresnel zone plates for improved resolution and efficiency in x-ray microscopy," J. Synchrotron Radiat. **25**(4), 1048–1059 (2018).
17. S. J. Goh, H. M. J. Bastiaens, B. Vratzov, *et al.*, "Fabrication and characterization of free-standing, high-line-density transmission gratings for the vacuum uv to soft x-ray range," Opt. Express **23**(4), 4421–4434 (2015).
18. I. Babenko, Y. Mostafa, Z. Bouza, *et al.*, "Spectral and spatial resolution of an extreme ultraviolet broadband imaging spectrometer based on dispersion-matched zone plates," AIP Adv. **14**(10), 1–6 (2024).
19. K. Matsushima and T. Shimobaba, "Band-limited angular spectrum method for numerical simulation of free-space propagation in far and near fields," Opt. Express **17**(22), 19662–19673 (2009).
20. J. W. Goodman, "Introduction to fourier optics," (1969).
21. R. Schupp, F. Torretti, R. Meijer, *et al.*, "Efficient generation of extreme ultraviolet light from Nd:YAG-driven microdroplet-tin plasma," Phys. Rev. Appl. **12**(1), 014010 (2019).
22. Z. Bouza, "Developments for broadband spectral and spatial characterization of tin plasma light sources for euv lithography," Phd thesis, (Vrije Universiteit, 2023).
23. F. Shen and A. Wang, "Fast-fourier-transform based numerical integration method for the Rayleigh-Sommerfeld diffraction formula," Appl. Opt. **45**(6), 1102–1110 (2006).
24. F. Torretti, J. Sheil, R. Schupp, *et al.*, "Prominent radiative contributions from multiply-excited states in laser-produced tin plasma for nanolithography," Nat. Commun. **11**(1), 2334 (2020).
25. V. Bakshi, *Photon sources for lithography and metrology* (SPIE Press, 2023).
26. M. Bayraktar, H. M. J. Bastiaens, C. Bruineman, *et al.*, "Broadband transmission grating spectrometer for measuring the emission spectrum of EUV sources," NEVAC blad **54**, 14–19 (2016).
27. W. H. Richardson, "Bayesian-based iterative method of image restoration," J. Opt. Soc. Am. **62**(1), 55–59 (1972).
28. L. B. Lucy, "An iterative technique for the rectification of observed distributions," Astronomical Journal **79**, 745 (1974).
29. M. Ingaramo, A. G. York, E. Hoogendoorn, *et al.*, "Richardson–Lucy deconvolution as a general tool for combining images with complementary strengths," ChemPhysChem **15**(4), 794–800 (2014).
30. Y. Liu, S. Panezai, Y. Wang, *et al.*, "Noise amplification and ill-convergence of Richardson–Lucy deconvolution," Nat. Commun. **16**(1), 911 (2025).
31. G. L. Almeida, M. I. Silvani, E. S. Souza, *et al.*, "A stopping criterion to halt iterations at the Richardson-Lucy deconvolution of radiographic images," J. Phys.: Conf. Ser. **630**, 012003 (2015).

Optics EXPRESS

32. S. Prasad, "Statistical-information-based performance criteria for Richardson–Lucy image deblurring," J. Opt. Soc. Am. A **19**(7), 1286–1296 (2002).
33. S. J. J. de Lange, D. J. Hemminga, Y. Mostafa, *et al.*, "Modeling the hundreds-of-nanoseconds-long irradiation of tin droplets with a 2 μm-wavelength laser for future euv lithography," Plasma Sources Sci. Technol. **33**(10), 105003 (2024).
34. Y. Mostafa, L. Behnke, D. J. Engels, *et al.*, "Mass use in 2 μm laser-driven tin plasma using sheet targets," J. Appl. Phys. **138**(14), 143304 (2025).